Computers in Biology and Medicine 115 (2019) 103478

Contents lists available at ScienceDirect

Computers in Biology and Medicine

journal homepage: http://www.elsevier.com/locate/compbiomed

Probability density function based modeling of spatial feature variation in capsule endoscopy data for automatic bleeding detection

Amit Kumar Kundu, Shaikh Anowarul Fattah *

Department of Electrical and Electronic Engineering, Bangladesh University of Engineering and Technology, Bangladesh

ARTICLE INFO

Keywords:
Bleeding detection
Bleeding zone localization
Pixels of interest
Rayleigh probability density function (PDF)
Support vector machine
Wireless capsule endoscopy

ABSTRACT

Wireless capsule endoscopy (WCE) is a video technology to inspect abnormalities, like bleeding in the gastrointestinal tract. In order to avoid a complex and long duration manual review process, automatic bleeding detection schemes are developed that mainly utilize features extracted from WCE images. In feature-based bleeding detection schemes, either global features are used which produce averaged characteristics ignoring the effect of smaller bleeding regions or local features are utilized that cause large feature dimension. In this paper, pixels of interest (POI) in a given WCE image are determined using a linear separation scheme, local spatial features are then extracted from the POI and finally, a suitable characteristic probability density function (PDF) is fitted over the resulting feature space. The proposed PDF model fitting based approach not only reduces the computational complexity but also offers more consistent representation of a class. Details analysis are carried out to find the best suitable PDF and it is found that fitting of Rayleigh PDF model to the local spatial features is best suited for bleeding detection. For the purpose of classification, the fitted PDF parameters are used as features in the supervised support vector machine classifier. Pixels residing in the close vicinity of the POI are further classified with the help of an unsupervised clustering-based scheme to extract more precise bleeding regions. A large number of WCE images obtained from 30 publicly available WCE videos are used for performance evaluation of the proposed scheme and the effects on classification performance due to the changes in PDF models, block statistics, color spaces, and classifiers are experimentally analyzed. The proposed scheme shows satisfactory performance in terms of sensitivity (97.55%), specificity (96.59%) and accuracy (96.77%) and the results obtained by the proposed method outperforms the results reported for some state-of-the-art methods.

1. Introduction

Detecting abnormalities like bleeding in the gastrointestinal (GI) tract via manual inspection of wireless capsule endoscopy (WCE) videos requires a substantial amount of time [1–4]. Therefore, automatic bleeding detection from WCE videos has received great attention from researchers for its clinical importance [5,6]. In this regard, many computer-aided bleeding detection techniques are available in the literature based on pixel-level or block-level statistics. The suspected blood indicator (SBI) is reported to be one of the first attempts to detect WCE bleeding images with moderate accuracy although it does not achieve the main goal of reduced interpretation time [7–9]. In Ref. [10], a region growing based bleeding detection method is proposed utilizing some statistical features, where a major limitation is the necessity for manual identification of a bleeding region at the beginning. In Ref. [11], a probabilistic neural network is employed for bleeding detection based on the features extracted from pixel intensity values. In Refs. [12,13], to detect bleeding, features are extracted from salient points. Instead of directly using pixel-level operations, in Refs. [14–16], block-based bleeding detection methods are proposed. In Refs. [17–19], deep learning based schemes are implemented for bleeding detection. In the model proposed by Ref. [20], the training requires high computational scope and a huge computation time to get the trained model. Moreover, a large number of images are required for training purposes. However, in medical image analysis, a good number of images may not become available for training [21]. Recently, therefore, in Ref. [22], differential cluster-based features are extracted, and in Ref. [23], an adaptive locality-constrained linear coding scheme is employed for feature-based abnormality detection. In many of these methods, due to considering the whole image, quality features may not be obtained for images having small bleeding zones. In addition, this involves huge computational burden. One possible solution is to extract features from a preliminary

* Corresponding author.
E-mail addresses: amit31416@gmail.com (A.K. Kundu), fattah@eee.buet.ac.bd (S.A. Fattah).

https://doi.org/10.1016/j.compbiomed.2019.103478
Received 10 January 2019; Received in revised form 30 September 2019; Accepted 30 September 2019
Available online 3 October 2019

selection of pixels of interest (POI). In this regard, a precise extraction of POI can ensure better features for classification. In Ref. [24], a criteria is proposed for initial POI selection before extracting the feature. Alternatively, histogram-based features are widely used for bleeding detection [25–28]. In the case of histogram-based approaches, the performance depends on the number of bins chosen, and it can be difficult to choose an optimum bin number in a real-life implementation. Many of these methods involve large feature dimensions. In Refs. [29,30], principal component analysis (PCA) based schemes are introduced to reduce the feature dimension. However, while a histogram represents the feature variation, it cannot directly provide parameterization of the variation pattern, but the use of a probability density function (PDF) fitted on local features can capture the inherent variation pattern more precisely. After successfully detecting bleeding images from WCE videos, an automatic and precise bleeding zone identification in that image is an essential and challenging task, but it can provide numerous aids for physicians, such as quick visualization of the bleeding regions and exploration of the consecutive changes of bleeding characteristics in consecutive images of WCE video. To address this issue, in Refs. [24,26], methods are proposed for automatic bleeding region identification from WCE bleeding images. However, developing a precise bleeding zone localization scheme for real-time implementation is still a challenge. Hence, a unified method that can detect bleeding images utilizing the inherent feature variation pattern and, at the same time, extract bleeding regions in real time is still in great demand.

The objectives of this paper are to develop an efficient scheme based on characteristic PDF fitting of POI statistics for detecting bleeding images and to propose a cluster-based approach for precisely extracting the corresponding bleeding regions. First, a linear separation scheme is employed for extracting the precise POI. Next, surrounding blocks of all POI are considered to compute the local spatial features such as mean, median, mode, minimum, and maximum (later termed POI statistics) in R, G, and B planes. Unlike conventional methods, instead of directly using the POI statistics or their histograms as features, we propose to fit a characteristic PDF suitable for modeling the spatial feature variation patterns. Such a PDF model fitting based approach can offer very low feature dimensions with a more consistent class representation. To the best of our knowledge, none of the reported computer-aided bleeding detection schemes utilize the feature variation pattern by fitting a PDF. After that, the characteristic parameters of the fitted PDF are used as features for bleeding frame classification using a support vector machine (SVM) classifier. Later, from the detected bleeding images, a K-means clustering-based scheme is proposed using the characteristic local features of critical pixels, residing just outside the boundary region formed by POI, to classify the critical pixels for extracting precise bleeding regions. Classification performance is tested on a publicly available WCE video database. Finally, the bleeding detection scheme is analyzed for performance evaluation in continuous WCE videos.

The rest of the paper is organized as follows. Section 2 is the materials and methodology section, where Section 2.2 presents the proposed bleeding image detection technique, and in Section 2.3, the proposed bleeding zone localization scheme is described in detail. Section 3 describes the results of the proposed scheme with performance comparisons. Concluding remarks are presented in Section 4.

2. Materials and methodology

2.1. Dataset

In this work, 30 WCE videos are collected from the widely used database available in Ref. [31]. Images in bleeding videos are manually commented as bleeding or non-bleeding by expert physicians. For bleeding image detection, 2350 WCE images are extracted from the videos, where 450 show signs of bleeding, and the rest of them are non-bleeding images. Examples of some WCE bleeding and non-bleeding images are shown in Fig. 1. Fig. 1 (a) and 1(b) represent the WCE bleeding images, whereas Fig. 1(c) and (d) represent the non-bleeding images. The initial *RGB* image size is 576×576 pixels. After discarding the square-shaped black pixels, the image size becomes 512×512. Next, the information bearing region is obtained by removing the corner black pixels. First, for all experiments, the preprocessing technique is applied to each given WCE image.

2.2. Proposed bleeding image detection scheme

The steps involved in detecting bleeding images from WCE videos are as follows: extraction of POI in a WCE image, computation of POI statistics, fitting of POI statistics with a suitable PDF, proposed feature extraction from the fitted PDF, and classification with the SVM classifier. Fig. 2 illustrates the steps in bleeding frame detection.

2.2.1. Extraction of local spatial features from pixels of interest (POI)

In a given square-shaped WCE image, the central information bearing circular region is surrounded by undesired peripheral black pixels, as demonstrated in Fig. 1. Therefore, a preprocessing scheme is employed by discarding all the surrounding black pixels. Next, the descriptive features from a preprocessed WCE image (denoted by I) need to be extracted for classifying the bleeding and non-bleeding images. However, in many bleeding detection algorithms, the features are extracted from the whole image [22,23,26]. Bleeding regions in bleeding images are present in varying shapes and sizes and are absent in non-bleeding images. The feature quality for bleeding image detection degrades if features are extracted from the whole bleeding image having large non-bleeding regions. Hence, instead of considering the whole image, in Ref. [24], some preliminary bleeding-like pixels are selected for better distinguishable feature extraction and for involving less computational burden. Therefore, in this paper, preliminary POI are selected for feature extraction rather than utilizing the whole image. Let R, G, and B be the red, green, and blue color channels of image I. The POI selection scheme employed here is as follows:

$$S_{POI} = \{(i,j)|R(i,j) \geq m \times B(i,j)\} \cap \{(i,j)|R(i,j) \geq n \times G(i,j)\}, \quad (1)$$

where S_{POI} is the set of POI in image I, and (i,j) is the coordinate of a pixel. This linear POI extraction criteria is simple but fast and efficient in terms of extracting the bleeding-like pixels as mentioned in Ref. [24]. The appropriate values of m and n are obtained after experimenting with various m and n values on the proposed bleeding image detection algorithm. $S'_{POI} = I - S_{POI}$ is the set of coordinates which are not selected as POI in image I.

Fig. 3 illustrates the POI extraction procedure. Fig. 3(a) and (c) represent, respectively, a preprocessed bleeding image and a non-bleeding image, whereas the extracted POI (using $m = 3.25$ and $n = 2.25$) of the corresponding images are demonstrated in Fig. 3(b) and (d), respectively. However, the extracted POI do not guarantee the classification of a test image. For example, even for a non-bleeding image, small or scattered pixels may be selected because of the presence of bleeding-like pixels. Therefore, in order to determine whether an image is bleeding or not, features must be extracted from the selected POI. Next, to extract the characteristic local spatial features from POI (termed "POI statistics"), the surrounding blocks of POI are considered. For extracting the POI statistics, different features, such as mean, maximum, mode, minimum, and median values of the surrounding blocks of the POI are calculated at R, G, and B planes. For example, $\mathbf{x}_{\mathbf{R}_{\text{Mean}}}$ is a vector consisting of the mean values of blocks surrounding $\forall(i,j) \in S_{POI}$ at R plane, and so on.

2.2.2. Proposed probability density function (PDF) fitting based feature extraction

The performance of a bleeding detection scheme depends on the quality of extracted features. In capsule endoscopy, to distinguish

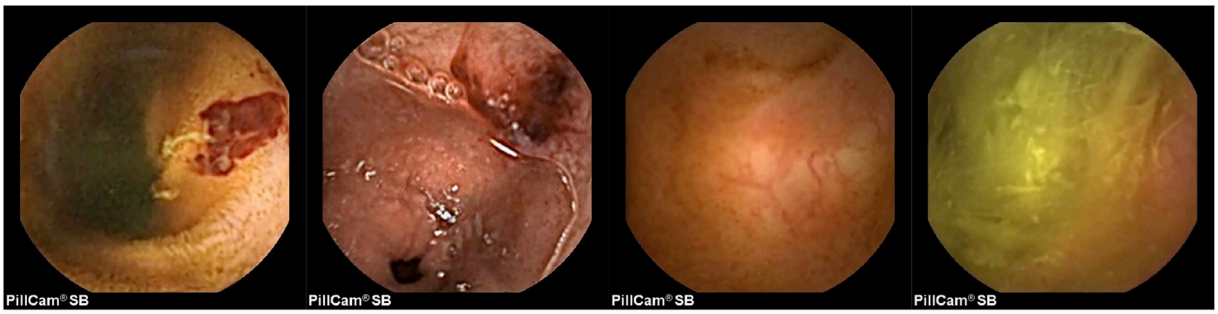

Fig. 1. Typical wireless capsule endoscopy (WCE) images: (a) and (b) WCE bleeding images. (c) and (d) WCE non-bleeding images.

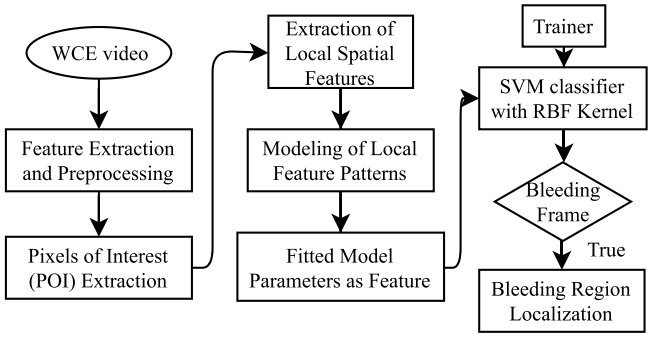

Fig. 2. The steps involved in the proposed method. WCE = wireless capsule endoscopy; SVM = support vector machine; RBF = radial basis function.

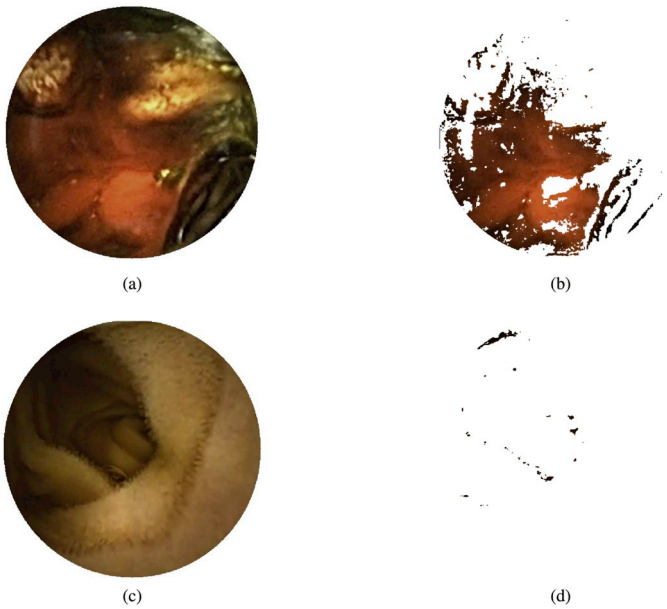

Fig. 3. Pixels of interest (POI) extraction. (a) Preprocessed bleeding image. (b) Extracted POI of the bleeding image. (c) Preprocessed non-bleeding image. (d) Extracted POI of the non-bleeding image.

bleeding and non-bleeding images from color information, one can use the extracted POI statistics or their histogram bin frequencies as features. In the case of histogram based features, the feature dimension will be very high. Again, the histogram represents the frequency variation pattern of POI statistics but cannot directly provide parameterization of the inherent variation pattern. Therefore, to reduce the feature dimension and to extract the characteristic nature of different POI statistics, the frequency variation profiles of POI statistics can be utilized. In this way, only a few characteristic representations of the frequency variation patterns can represent the whole nature of the image, which can lead to better classification performance. Hence, it is expected that the use of different PDFs to describe the expected variation pattern of POI statistics should help to extract quality features for classifying bleeding and non-bleeding images. Here, the PDF fitting refers to the development of analytic representation for explaining the distribution of POI statistics in an image. Therefore, in this paper, we propose to fit a characteristic PDF suitable for modeling each of the POI statistics. Such a PDF fitting based bleeding detection scheme has several advantages.

- First, it offers a very low feature dimension in comparison to histogram based approaches, where all bin frequencies are used as features.
- Second, in histogram-based approaches, the performance of the method is uncertain as it depends on the number of bins, and it is difficult to choose an optimum bin number in a real-life implementation. However, in a PDF fitting-based approach, only a few fitted parameters are extracted, which can capture the inherent variation pattern of the POI statistics with a consistent class representation.

Finally, the characteristic parameters of the fitted PDF are used for bleeding frame classification, which greatly reduces the computational cost. The PDF of the POI statistics (x) can be approximated by different well-known PDFs, as mentioned in Table 1 [32].

To extract features from the POI statistics, their histograms are approximated by a reasonably close PDF. Here, the histograms are constructed using the Freedman-Diaconis rule [33]. To demonstrate the model-fitting performance using different PDFs, three PDFs are considered, as shown in Fig. 4. These are normal distribution, Rayleigh distribution, and exponential distribution. The empirical histograms of different POI statistics in the R plane for the three PDFs are presented in Fig. 4. In this figure, it can be seen that the Rayleigh distribution fits best the empirical histograms. However, it should be mentioned that a similar analysis is found in the cases of G and B plane histogram patterns. For demonstration purposes, 100 bleeding and 100 non-bleeding images are randomly chosen for consideration of investigating the discriminating nature of the fitted Rayleigh PDF parameters for

Table 1
Different probability density functions (PDFs).

Distribution Name	Equation	Fitted Parameter(s)
Rayleigh	$f(x;\sigma) = \frac{x}{\sigma^2} e^{-x^2/(2\sigma^2)}, \quad x \geq 0$	σ
Normal	$f(x;\mu,\sigma^2) = \frac{1}{\sqrt{2\pi\sigma^2}} e^{-\frac{(x-\mu)^2}{2\sigma^2}}$	μ, σ
Exponential	$f(x;\lambda) = \begin{cases} \lambda e^{-\lambda x} & ,x \geq 0, \\ 0 & ,x < 0. \end{cases}$	λ

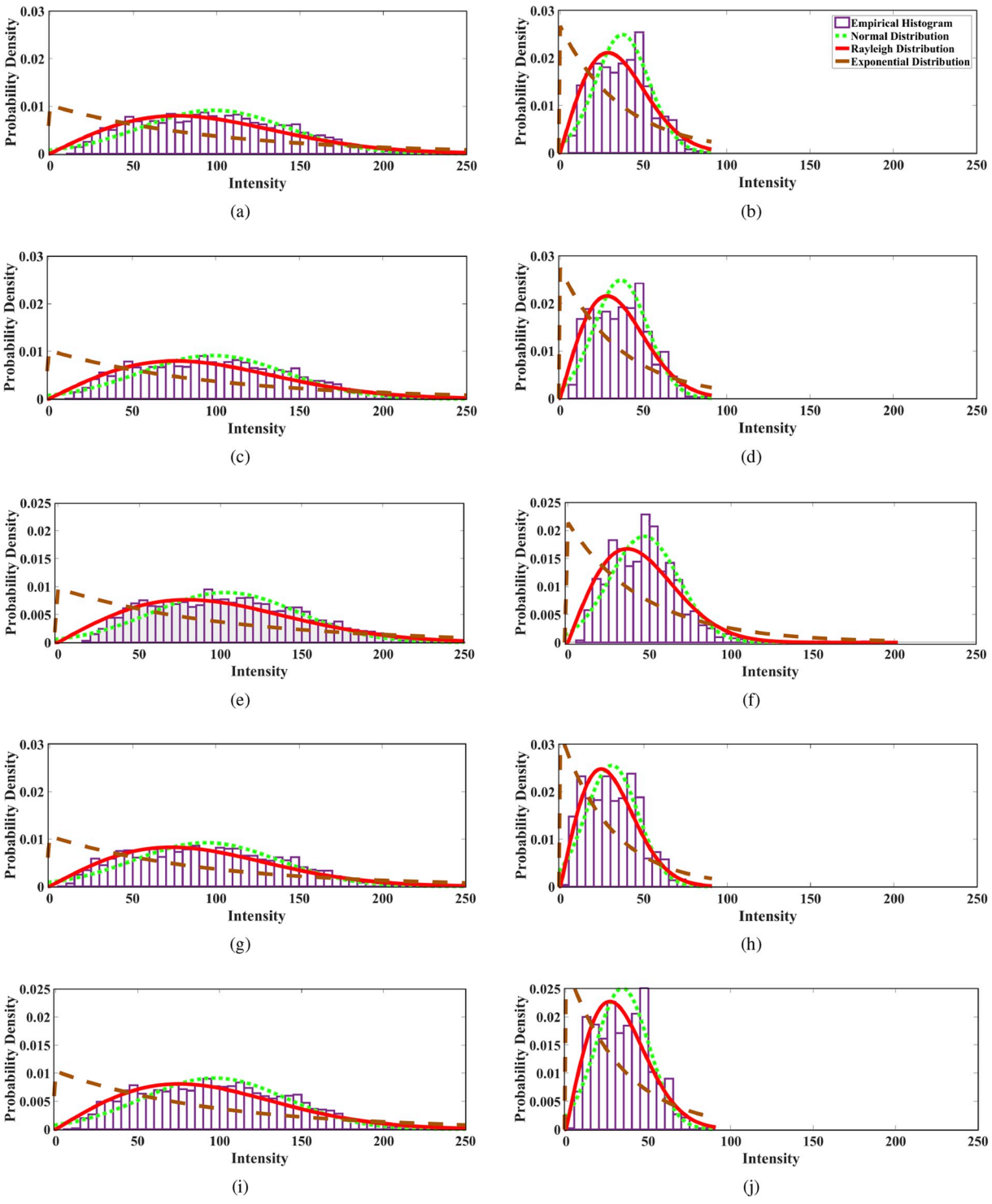

Fig. 4. Model representations of spatial feature variation patterns. Figures in the rows represent the variation patterns of, respectively, block mean, median, maximum, minimum, and mode calculated from the pixels of interest (POI) at the *R* plane. The left column represents the patterns for a bleeding image, and the right column is for a non-bleeding image. Each figure has four curves, such as the empirical histogram of spatial feature, normal probability density function (PDF), Rayleigh PDF, and exponential PDF fitted to the feature variation pattern.

classification. Fig. 5 shows the box plots of the Rayleigh fitted model parameters for different POI statistics, such as mean, median, minimum, maximum, and mode, in the *R* plane. Similar box plots are found for the *G* and *B* planes. Again, to demonstrate the distinctiveness of the fitted Rayleigh PDF parameters in classifying bleeding and non-bleeding images, 100 bleeding and 100 non-bleeding randomly chosen images are considered for performing the statistical significance *t*-test 10 times, and the extracted mean *p* values are shown in Fig. 6. The *p* values are very small for all of the extracted parameters from the Rayleigh PDF fitted to different local features. Therefore, is it evident from these figures that the fitted parameters of the Rayleigh PDF for different POI statistics imply a significant amount of class separation and can be considered strong features for classifying bleeding and non-bleeding images. Moreover, by choosing the fitted parameters as features, the

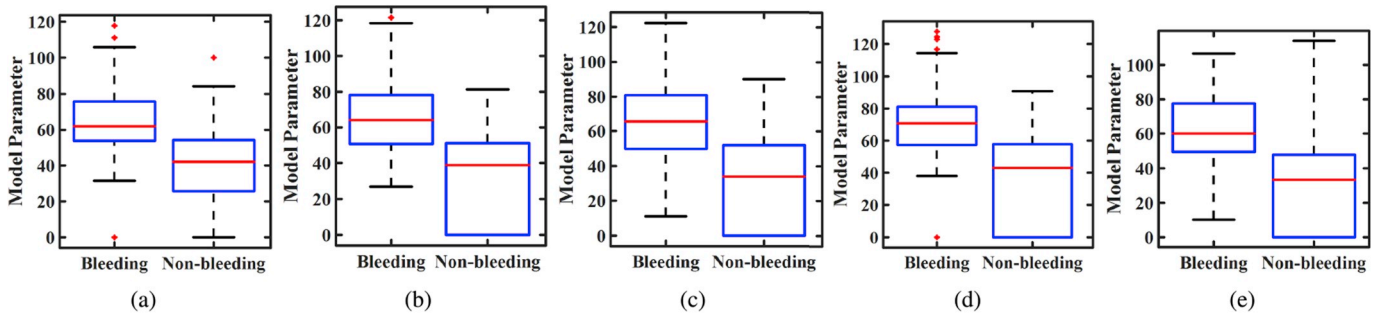

Fig. 5. Box plot of Rayleigh probability density function (PDF) parameters fitted on different pixels of interest (POI) statistics: (a) $\sigma_{R_{Mean}}$; (b) $\sigma_{R_{Median}}$; (c) $\sigma_{R_{Mode}}$; (d) $\sigma_{R_{Max}}$; (e) $\sigma_{R_{Min}}$ in the R plane of randomly chosen 100 bleeding and 100 non-bleeding images.

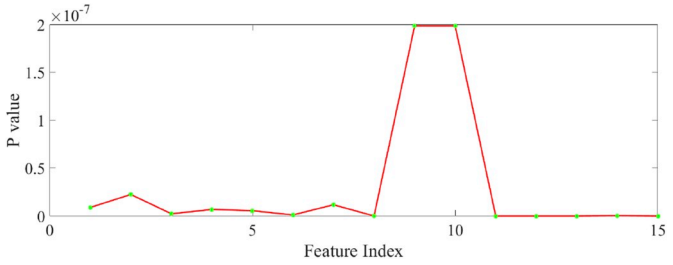

Fig. 6. Mean p values from t-test of Rayleigh probability density function (PDF) parameters fitted to different local features.

computational cost involved in classification will also be greatly reduced because of a huge reduction in feature dimensions. In order to acquire the final feature vector $\mathbf{F}$, the feature vectors $\mathbf{F_R}$, $\mathbf{F_G}$, and $\mathbf{F_B}$ at three color planes consisting of the fitted parameters of POI statistics (mean, median, mode, maximum, and minimum) are concatenated as depicted in Equation (2) through (5).

$$\mathbf{F_R} = [\sigma_{R_{Mean}} \quad \sigma_{R_{Median}} \quad \sigma_{R_{Min}} \quad \sigma_{R_{Max}} \quad \sigma_{R_{Mode}}] \tag{2}$$

$$\mathbf{F_G} = [\sigma_{G_{Mean}} \quad \sigma_{G_{Median}} \quad \sigma_{G_{Min}} \quad \sigma_{G_{Max}} \quad \sigma_{G_{Mode}}] \tag{3}$$

$$\mathbf{F_B} = [\sigma_{B_{Mean}} \quad \sigma_{B_{Median}} \quad \sigma_{B_{Min}} \quad \sigma_{B_{Max}} \quad \sigma_{B_{Mode}}] \tag{4}$$

$$\mathbf{F} = [\mathbf{F_R} \quad \mathbf{F_G} \quad \mathbf{F_B}] \tag{5}$$

where, $\sigma_{R_{Mean}}$ is the fitted parameter when a Rayleigh PDF is fitted to the mean values ($\mathbf{x_{R_{Mean}}}$) of blocks surrounding $\forall(i,j) \in S_{POI}$ at the R plane and so on.

2.2.3. Support vector machine (SVM) classifier

The supervised SVM is a high-performance sparse classifier for two-class problems [34]. The objective function creates a maximum margin to separate the two opposite classes and reduces the error at the same time. The key component in SVM learning is to identify the set of support vectors from the marginal hyper-planes or from the outlier patterns, which are useful for shaping the (linear or nonlinear) decision boundary. Considering a kernel function that maps the feature space into a higher dimensional feature space, non-linear boundaries can be drawn, which become more effective for most supervised classification problems. Hence, in this paper, the SVM classifier is employed for bleeding frame detection from WCE videos.

2.3. Proposed bleeding region detection scheme

After the successful detection of a bleeding image from WCE videos, an automatic and precise bleeding zone identification in that image is a challenging task, but one that can provide numerous aids for the physicians. In what follows, a proposed scheme of automatic bleeding region extraction from bleeding images is presented in detail.

The POI extraction scheme described in Section 2.2.1 significantly helps in achieving quality features to detect bleeding images and offers a fairly good estimate of bleeding regions. However, in order to obtain a very precise bleeding region, it is important to check the candidacy of a few more pixels that were not included in the POI set (S_{POI}). Nevertheless, it is impossible to recheck all other pixels that are not in S_{POI} for real-time computation of bleeding regions. It can be observed that the extracted POI, in most cases, form a bounded region. The pixels that are close to the border region formed by the POI (later termed critical pixels) need to be checked again to incorporate any possible bleeding candidate pixel in the bleeding region, as they may possess characteristics similar to bleeding. The proposed bleeding region extraction scheme has the following advantages:

- The scheme involves less computation. Moreover, it utilizes variables from memory that were already computed in the bleeding image detection stage. Therefore, the bleeding regions are extracted in real time.
- The scheme considers a few other probable bleeding candidate pixels outside of the POI for further examination so that more precise bleeding zones are extracted.

2.3.1. Detection of critical pixels

In order to detect the critical pixels, a binary image is first formed using the following criteria:

$$I_B(i,j) = \begin{cases} 1, & (i,j) \in S_{POI} \\ 0, & (i,j) \in S'_{POI} \end{cases} \tag{6}$$

Then, the edge (or boundary) formed by the POI is determined by applying the Sobel algorithm to the binary image I_B. Next, a $p \times p$ block is considered, keeping each edge pixels in the center. Let Q_k be the set of coordinates of the surrounding $p \times p$ block of k-th edge pixels, for $k = 1, 2, 3, \ldots, M$, where M is the total number of edge pixels. Now, Q_k contains pixels from both S_{POI} and S'_{POI}. Let Q_{rk} be the set of coordinates from S_{POI}, and Q_{nk} is the set of coordinates from S'_{POI} residing in the k-th block. Q_{nk} is determined such that $Q_{nk} = \{(i,j) \in Q_k | I_B(i,j) = 0\}$, which means Q_{nk} contains the coordinates where the binary image intensity is zero, and as a result, the pixels are not POI. Similarly, $Q_{rk} = \{(i,j) \in Q_k | I_B(i,j) = 1\}$, and these pixels are already in the S_{POI}, and hence, they do not require further testing. The situation is illustrated in Fig. 7, where each square is used to represent a pixel, and a 7×7 block is considered around a center edge pixel. The edge is represented with the help of blue colored squares. The pixels under the edge pixels are the POI ($I_B(i,j) = 1$). However, the pixels in S'_{POI} (the upper and left pixels as shown in Fig. 7) do not satisfy the POI extraction criteria ($I_B(i,j) = 0$) and, hence, are considered for further testing. After that, $Q_n = \bigcup_{k=1}^{M} Q_{nk}$ is determined as the set of critical pixels.

2.3.2. Proposed clustering-based critical pixel classification

After acquiring the critical pixels, the characteristic local spatial features of these pixels must be extracted for classification. For extracting the local features of critical pixels such as mean, maximum, mode, minimum, and median values of the surrounding blocks, $\forall(i,j) \in Q_n$ are calculated at the R, G, and B planes using the given RGB image I. Moreover, from the bleeding image detection step, the POI statistics of the bleeding image are already in memory. Therefore, the average values (μ) of all POI statistics are computed, for example, $\mu_{R_{Mean}} = mean(\mathbf{x}_{\mathbf{R_{Mean}}})$ and so on. Now, a vector $\mathbf{C}_0$ is constructed where $\mathbf{C}_0 = [\mu_{R_{Mean}} \quad \mu_{R_{Median}} \quad \dots \quad \mu_{B_{Mode}}]$. Next, the critical pixels are divided into K groups by applying a K-means clustering algorithm [35] using the calculated local features of critical pixels. The K-means clustering algorithm provides K cluster centers ($\mathbf{C}_1, \mathbf{C}_2, \dots, \mathbf{C_K}$) and assigns the data points in a particular cluster according to their mean value distribution. The pixels residing in the cluster with a cluster center closer to $\mathbf{C}_0$ are more likely to be bleeding pixels. Hence, the cluster having $min(\| \mathbf{C}_1 - \mathbf{C}_0\|_2, \| \mathbf{C}_2 - \mathbf{C}_0\|_2, \dots, \| \mathbf{C_K} - \mathbf{C}_0\|_2,)$ is chosen as the desired cluster, where the symbol $||\cdot||_2$ is used to express the Euclidean norm. The pixels of the desired cluster are incorporated in the bleeding region along with the previously extracted POI. The candidacy checking scheme of critical pixels is useful for incorporation of any probable bleeding candidates in the desired bleeding zone and helps to improve the bleeding zone detection accuracy.

Moreover, the extracted bleeding zone may not be continuous in shape. However, in reality, the bleeding zone is continuous and smooth. In the proposed bleeding region detection scheme, two stages of morphological operations, namely morphological erosion and morphological dilation, are carried out after classifying the critical pixels for smoothing the extracted bleeding regions [36]. Algorithm 1 summarizes the steps of the proposed bleeding region detection algorithm.

Algorithm 1. Proposed bleeding zone localization algorithm.

Input: A bleeding image (I), extracted pixels of interest (POI) (S_{POI}), POI statistics.

Output: Extracted bleeding zone.

Step 1: Select the block size, p
Step 2: Determine the binary image (I_B) from S_{POI} and S'_{POI} using Equation (6).
Step 3: Extract critical pixels (Q_n) as mentioned in Section 2.3.1.
Step 4: Extract characteristic local spatial features of critical pixels.
Step 5: Compute $\mathbf{C}_0$ from all POI statistics.
Step 6: Apply K-means clustering algorithm using the calculated local features of the critical pixels (Q_n). Determine the cluster centers $\mathbf{C}_1, \mathbf{C}_2, \dots \mathbf{C_K}$.

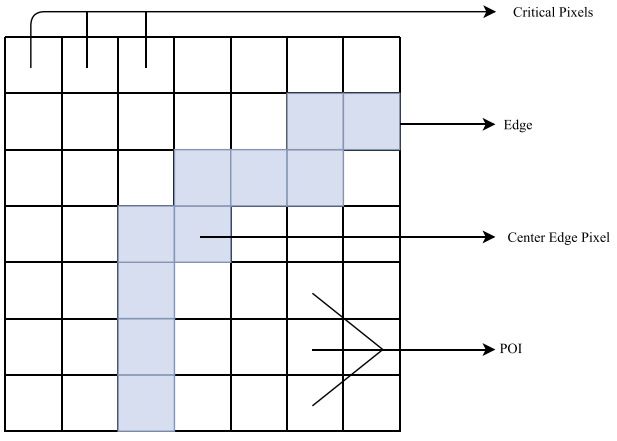

Fig. 7. Determination of critical pixels.

Step 7: Determine the cluster with a center of $min(||\mathbf{C}_1 - \mathbf{C}_0||_2, ||\mathbf{C}_2 - \mathbf{C}_0||_2, \dots, ||\mathbf{C_K} - \mathbf{C}_0||_2)$.
Step 8: Include the pixels of the chosen cluster along with POI to form a binary image.
Step 9: Return bleeding zone in a bleeding image after morphological erosion and dilation of the binary image.

3. Results and discussion

This section presents the experimental results obtained from the proposed method in three aspects: 1) bleeding image detection performance, 2) bleeding zone localization performance, and 3) performance in continuous WCE clips. Along with performance results, the performance evaluation criteria are also presented.

3.1. Goodness of fit: Bayesian information criterion (BIC)

Bayesian information criterion (BIC) is a criterion for model selection among a finite set of PDF models, where the PDF model having the lowest BIC value is chosen [37]. To compare the fitting performance of different PDFs, the average BIC values of fitted PDFs using 15 different local features (block mean, median, mode, maximum, and minimum at the R, G and, B planes) are shown in Fig. 8. It is observed from the figure that in most cases, the fitting performance of Rayleigh distribution outperforms the other distributions.

3.2. Goodness of feature: geometric separability index (GSI)

In order to demonstrate the quality of the extracted features for bleeding image classification, the geometric separability index (GSI) is used, which is defined in Ref. [38] as

$$GSI = \frac{\sum_{i=1}^{N}\left(f(\mathbf{F_i}) + f\left(\mathbf{F_i}^T\right) + 1\right) mod\ 2)}{N} \tag{7}$$

Here, $f(\cdot)$ is the binary class label, $\mathbf{F_i}^T$ is the nearest neighbor of any i-th feature vector $\mathbf{F_i}$, and N is the total number of images. For well-separated features, the GSI value will be close to 1, and a low GSI value indicates overlapping characteristics [39]. The GSI values of the proposed PDF fitting based features of different distributions are listed in Table 2. It can be clearly seen in Table 2 that, except for the Student-t distribution, all the other PDFs offer good quality of extracted features, which implies the proposed PDF fitting based scheme is good.

3.3. Performance evaluation criteria

For classification of bleeding and non-bleeding images, standard performance measures, namely sensitivity, specificity, and accuracy [40], are used, and for bleeding zone localization, false negative ratio (FNR), false positive ratio (FPR), and precision are used [41]. The definitions are presented in Table 3. Here, in the case of bleeding images detected, N is used to indicate the number of images for a particular case. For example, N_{TP} represents the number of true positive image detected. For bleeding region detection, M is used to indicate the number of pixels for a particular case. For instance, M_{TP} represents the number of true positive pixels in a bleeding image.

3.4. Performance of bleeding image detection

In order to extract model fitting based features from POI statistics, the POI are first extracted from each preprocessed WCE image using the criteria provided in Equation (1). After that, statistical measures, such as mean, median, mode, minimum, and maximum values of surrounding 3×3 blocks $\forall(i,j) \in S_{POI}$ in the R, G, and B planes, are calculated. Finally, all POI statistics are individually fitted in a PDF and the fitted

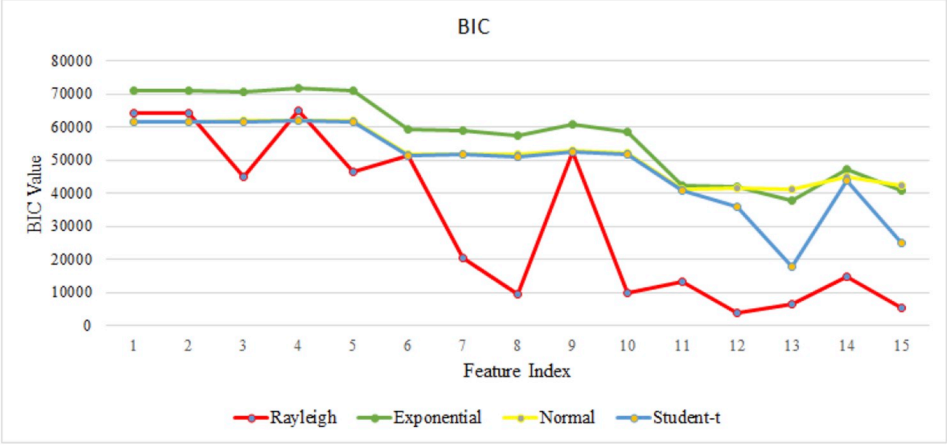

Fig. 8. Bayesian information criterion (BIC) values of different probability density functions (PDFs).

Table 2
Geometric separability index (GSI) of different distributions.

Distribution Name	Normal	Exponential	Rayleigh	Student-t	Gamma
GSI	0.9624	0.9791	0.9716	0.8776	0.9570

Table 3
Definition of performance measures. FNR = false positive ratio; FPR = false positive ratio.

for Bleeding Frame Detection	for Bleeding Zone Localization
$Sensitivity = \frac{N_{TP}}{N_{TP}+N_{FN}}$	$FNR = \frac{M_{FN}}{M_{FN}+M_{TP}}$
$Specificity = \frac{N_{TN}}{N_{TN}+N_{FP}}$	$FPR = \frac{M_{FP}}{M_{FP}+M_{TN}}$
$Accuracy = \frac{N_{TP}+N_{TN}}{N_{TP}+N_{FN}+N_{TN}+N_{FP}}$	$Precision = \frac{M_{TP}}{M_{TP}+M_{FP}}$

Table 4
Performance of the proposed method for various values of m and n.

m	n	Sensitivity (%)	Specificity (%)	Accuracy (%)
3.0	2.0	96.96	93.35	94.03
3.25	2.25	97.55	96.59	96.77
3.5	2.25	97.11	96.17	96.53
3.5	2.5	97.37	97.08	97.13

PDF parameters in cascade are used as features, followed by classification using the supervised SVM classifier. A tenfold cross-validation scheme is used to evaluate the image classification performance.

3.4.1. Effect of pixels of interest (POI) extraction parameters (m and n)

To find the appropriate values of m and n, different values of $m \in \{2.5, 2.75, \ldots, 3.5\}$ and $n \in \{1.5, 1.75, \ldots, 2.5\}$ are applied to extract the POI. Then, the POI statistics are fitted on the Rayleigh PDF, and classification is performed on the SVM classifier using a Gaussian radial basis function (RBF) kernel. Some of the best results are reported in Table 4.

Table 5
Performance of the proposed method using different distributions.

Distribution	Sensitivity	Specificity	Accuracy
Normal	94.39%	98.65%	97.83%
Poisson	**97.19%**	**96.11%**	**96.15%**
Exponential	**97.25%**	**96.63%**	**96.74%**
Rayleigh	**97.55%**	**96.59%**	**96.77%**
Gamma	89.35%	96.47%	95.12%
Student-t	77.32%	99.90%	91.98%

From Table 4, it can be seen that the performance indices are quite similar for the reported values of m and n. However, considering sensitivity as the most important, $m = 3.25$ and $n = 2.25$ are used in reporting performance of the proposed method in the rest of the paper, which results in an accuracy of 96.77%, a sensitivity of 97.55%, and a specificity of 96.59%. The average computational time of the proposed bleeding image detection scheme using an Intel core i-5 CPU @ 2.30 GHz clock, and 8.00 GB RAM requires 0.0756 s per sample for feature extraction and 0.000011395 s per sample for testing.

3.4.2. Effect of using different probability density functions (PDFs)

The performance of the proposed method is evaluated using different PDFs, namely Gaussian, Rayleigh, exponential, Poisson, gamma, and student-t distributions. The results presented in Table 5 demonstrate that Poisson distribution, Rayleigh distribution, and exponential distribution show similar good performances among all of the distributions. Moreover, in most images, no convergence is found when trying to fit the POI statistics to Weibull, lognormal and Nakagami distributions. Hence, in the rest of the paper, the remaining evaluations are performed using the Rayleigh distribution.

3.4.3. Effect of using individual color planes

Similarly, the performance of the proposed method is tested on individual R, G, and B planes, and the results are provided in Fig. 9. For example, in obtaining the performance of the proposed method in the R plane, $\mathbf{F_R}$ is used as the feature vector. Fig. 9 indicates that the result obtained using the PDF features from the R, G, and B planes in cascade outperforms the result obtained using features from individual planes.

3.4.4. Effect of using different pixels of interest (POI) statistics

Next, the effect of using different POI statistics individually and the

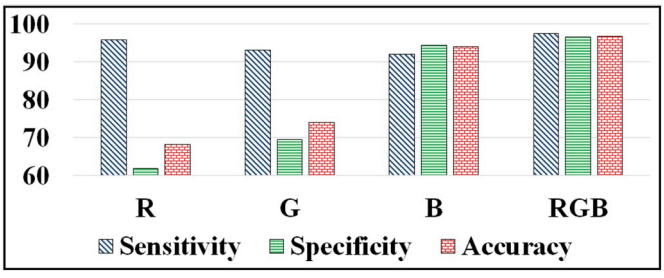

Fig. 9. Performance comparison of using Rayleigh probability density function (PDF) features from individual R, G, B color planes and using them in cascade. (For interpretation of the references to color in this figure legend, the reader is referred to the Web version of this article.)

Table 6
Performance of the proposed method using different block statistics.

Block Statistics	Sensitivity (%)	Specificity (%)	Accuracy (%)
Mean	92.16	88.33	89.06
Median	91.88	93.11	92.89
Minimum	93.89	94.13	94.09
Maximum	93.26	88.25	89.2
Mode	97.99	93.76	94.56
All Combined	**97.55**	**96.59**	**96.77**

effect of using them combined are given in Table 6. In obtaining the results shown in Table 6, the Rayleigh PDF is used, and classification is performed using the SVM classifier with the RBF kernel. For example, in reporting the results shown in the first row of Table 6, $[\sigma_{R_{Mean}} \ \sigma_{G_{Mean}} \ \sigma_{B_{Mean}}]$ is used as the feature vector. Results in Table 6 clearly show that using those five block statistics (mean, minimum, maximum, mode, and median) together as features leads to a better performance than using individual statistics. To acquire features of minimum correlation, a PCA is implemented using the proposed PDF-based features. The obtained sensitivity, specificity, and accuracy are 96.87%, 95.82% and 96.68%, respectively, which are slightly less than the results obtained by the proposed method. Moreover, instead of considering mean, minimum, maximum, mode, and median, one may also consider computing second-order POI statistics. For example, along with the block mean, second, third, and fourth order moments are chosen as local spatial features. The obtained results using these local features are as follows: sensitivity is 97.08%, specificity is 95.71%, and accuracy is 96.56%, which provides a similar performance as the proposed local features.

3.4.5. *Effect of using non-overlapping blocks*

For performance comparison, the local spatial features are extracted from non-overlapping blocks inside the POI set for modeling instead of using all the overlapping blocks surrounding the POI. The results are provided in Table 7. It can be seen that the use of non-overlapping blocks inside the POI shows quite satisfactory performance with less computation. However, taking all blocks inside the POI for modeling shows a better performance than taking non-overlapping blocks. But considering the computation involved, one can also use the non-overlapping blocks inside the POI for spatial feature extraction.

3.4.6. *Probability density function (PDF) fitting of pixels of interest (POI) intensities*

In order to compare between PDF fitting of POI statistics and PDF fitting of POI intensities, the proposed PDF fitting scheme is tested using pixel intensities instead of extracting the block statistics. The results are demonstrated in Table 8. One can use POI intensities for Poisson or exponential PDF fitting as it involves less computation. However, it is clear from Table 8 that the results obtained from PDF fitting of POI intensities cannot outperform the results obtained using PDF fitting of POI statistics.

3.4.7. *Performance of probability density function (PDF) fitting based feature extracted from the entire image*

Next, Table 9 shows the performance comparison of the proposed PDF fitting based approach using only POI statistics and using statistics from the whole image pixels. In the case of a whole image based approach, for PDF fitting, the surrounding block statistics $\forall(i,j) \in I$ are computed and fitted to the Rayleigh PDF, which is not feasible for real-time image classification. Moreover, using only POI statistics for PDF fitting shows a better result than using statistics from entire image pixels. Therefore, in this paper, a POI selection scheme is employed before feature extraction.

Table 7
Performance comparison between features extracted from overlapping blocks and non-overlapping blocks inside the pixels of interest (POI).

	Sensitivity	Specificity	Accuracy
Features from non-overlapping blocks	96.26%	96.17%	96.20%
Features from overlapping blocks	97.55%	96.59%	96.77%

Table 8
Performance of the probability density function (PDF) fitting-based feature extraction scheme using pixels of interest (POI) intensities.

Distribution	Sensitivity	Specificity	Accuracy
Normal	92.87%	92.73%	92.77%
Poisson	94.45%	93.88%	93.98%
Exponential	93.26%	92.98%	93.05%
Rayleigh	91.81%	94.10%	93.68%
Gamma	92.75%	92.64%	92.04%
Student-*t*	92.51%	94.61%	94.21%

Table 9
Performance comparison between pixels of interest (POI) based approach and whole image based approach.

	Sensitivity	Specificity	Accuracy
Using POI	97.55%	96.59%	96.77%
Using whole image	86.75%	90.18%	89.55%

3.4.8. *Effect of changing classifiers*

In Table 10, classification results of the proposed method using different classifiers, such as the K-nearest neighbors (KNN) classifier, the naive Bayesian (NB) classifier, the decision tree classifier, the random forest classifier, the SVM classifier (with linear and RBF kernel), and the artificial neural network (ANN) classifier, are shown. It is evident from the table that the SVM classifier outperforms all other classifiers in terms of all performance indices.

3.4.9. *Effect of using different color spaces*

In Fig. 10, comparison among results obtained using various color spaces such as *RGB*, *HSV*, *YIQ*, *YCbCr*, *CIE-LAB*, *CMYK*, and gray-scale image is demonstrated. Here, the POI are extracted in *RGB* space using Equation (1). Then, the POI intensities are converted to different color spaces before feature extraction. Fig. 10 demonstrates that sensitivity is higher in the *HSV* and *CIE-LAB* color domains. In the *YIQ* space, all three performance indices are significantly higher than the other color domains. Therefore, the proposed PDF fitting based feature extraction scheme can also be applied to several other color spaces, including *YIQ*, *HSV*, and *CIE-LAB*.

3.4.10. *Comparison of different methods*

To evaluate the proposed bleeding image detection scheme, it is compared with the methods proposed in Refs. [24,26,28], and the uniform local binary pattern (LBP) feature proposed in Ref. [15]. In the case of [15], the LBP features are extracted from the RGB color plane. In Ref. [24], histograms are computed using POI intensities in a normalized *G* plane. In Ref. [26], bleeding image is classified using unsupervised clustering based histogram features in a pixel domain using the whole image. In Ref. [28], histogram statistics are used as features in the RGB space. In these methods, the feature dimension is high because of using histogram bin frequencies as features. Moreover, one may think of implementing the proposed method without PDF modeling. In this case, instead of PDF fitting, statistical measures can be extracted from local spatial features for classification. For comparison, the mean and the variance of POI statistics are computed to construct the feature vector. All the methods are implemented using the same dataset mentioned in Section 2.1 and using the same SVM classifier. From the results presented in Table 11, it is evident that the proposed method performs better than the other methods in terms of all three performance indices,

Table 10
Performance comparison of the proposed method using different classifiers. KNN = K-nearest neighbors; NB = naive Bayesian; SVM = support vector machine; RBF = radial basis function; ANN = artificial neural network.

Classifier	KNN	NB	Decision Tree	Random Forest	SVM (Linear Kernel)	SVM (RBF Kernel)	ANN
Sensitivity	92.60%	89.01%	87.93%	90.86%	88.90%	**97.55%**	89.71%
Specificity	97.91%	83.38%	96.64%	96.31%	94.72%	**96.59%**	98.04%
Accuracy	96.89%	84.46%	94.78%	95.27%	93.29%	**96.77%**	96.45%

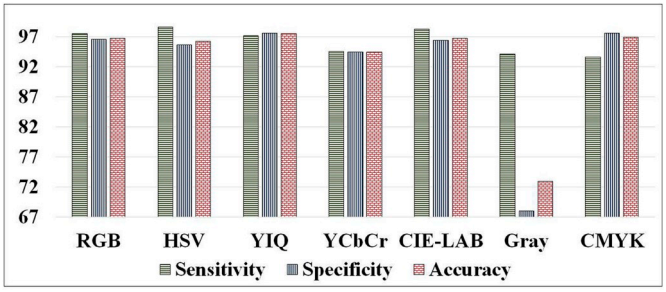

Fig. 10. Performance of the proposed method using different color spaces. (For interpretation of the references to color in this figure legend, the reader is referred to the Web version of this article.)

with a significant improvement in sensitivity. Therefore, it is clear that the PDF fitting based feature can greatly improve the performance of the bleeding frame detection method.

Besides using the tenfold cross-validation scheme, the proposed method is also implemented by randomly choosing 50% of the data as training, and the remaining 50% of the data are chosen for validation. Using the training data, a fivefold cross-validation scheme is used to select the optimum classifier parameter(s). Finally, by using the selected parameters, the final classifier model is trained to test the validation set. Similarly, the training set and validation set are switched, and the same procedure is followed. The mean sensitivity, specificity, and accuracy found on the validation set are, respectively, 97.48%, 96.32%, and 96.68%, which are similar to the reported results when a tenfold cross-validation is used for performance evaluation.

3.5. Performance of bleeding region detection scheme

The performance of the bleeding region extraction scheme is described in this Section considering 65 bleeding images, where the bleeding zones inside the images are marked by physicians. The POI set and its statistics of bleeding images are available from the bleeding image detection step. Using the POI and the given image, first, the set of critical pixels are extracted as mentioned in Section 2.3.1 for further examination of bleeding candidacy. After that, the critical pixels are classified using a clustering based approach, as mentioned in Section 2.3.2, in order to extract the desired bleeding region. In Fig. 11, the image outputs of the proposed bleeding zone localization scheme are presented using four images. The first column is the preprocessed bleeding images, while the second column shows the extracted POI of corresponding images, and the third column shows the localized bleeding zones. The final column shows the ground truth of bleeding zones labeled by the expert clinicians. It can be observed that the bleeding zones are accurately extracted by the proposed bleeding region detection scheme.

To evaluate the performance of the proposed bleeding region detection scheme, different values of $p \in \{3, 5, 7, 9, 11, 13\}$ with $K = 2$ are used, and the obtained results are reported in Table 12. It can be observed from the Table that $p = 9$ provides better performance than other values of p in terms of all performance indices, having a precision of 90.07%, FPR of 6.83%, and FNR of 30.79%. Higher values of p involve more computation. Hence, $p = 9$ is proposed in this paper. The reason for such a high numeric figure for FNR is that when the ground truths are marked by the physicians, they mark the image holistically and not pixel by pixel. For example, there may be 2%–5% disjointed bleeding pixels, but the physicians mark the regions as a continuous region. As a result, a few pixels will not be detected as bleeding in the proposed region localization scheme. Next, the bleeding region localization scheme is implemented using different values of $K \in \{2, 3, 4, 5\}$, and the obtained results are reported in Table 13. It can be seen in the table that the FNR is increasing with an increase in the value of K. Therefore, $K = 2$ is chosen in this paper. As the initial POI set provides a fair estimate of the bleeding region, the region localization scheme is also implemented in the RGB space without the K-means clustering step. Here, the bleeding region is formed by the set of initial POI in a bleeding WCE image, followed by the morphological operations. The obtained result is as follows: precision is 89.05%, FPR is 6.58%, and FNR is 35.70%. Hence, it is clear that the additional K-means clustering step is able to significantly improve the precision and FNR as more bleeding pixels are incorporated in the desired bleeding zone. Like the critical pixel classification, one may think of incorporating an additional refinement step to reduce the false positive pixels. Therefore, to reduce the false positive pixels, after classification of the critical pixels, a few more POI near the boundary regions are considered and classified using a separate K-means clustering in a similar way. The obtained precision, FPR, and FNR are, respectively, 90.31%, 4.51%, and 40.60%. We can observe from the results that even though FPR is improved by a slight margin, FNR is greatly increased. This is because a lot of bleeding pixels are falsely classified as normal pixels after applying the above-mentioned step. Therefore, classification of a few more POI near the boundary region is not considered in the proposed method. Next, the proposed region detection scheme is compared with the methods proposed in Refs. [24, 26], in Table 14. A two-stage saliency extraction scheme is proposed in Ref. [26] to localize the bleeding areas, which involves more computation as the scheme combines various color spaces. In Ref. [24], bleeding region is extracted using a two-stage linear separation criteria in a normalized RGB space [24]. only includes POI in the bleeding zone without considering any potential critical pixels for further examination. The proposed bleeding region localization method performs better than the methods in Refs. [24,26] in terms of precision and FNR. Moreover, to compare the performance of the proposed bleeding region localization scheme with the methods proposed in Refs. [16,42], a publicly available dataset [43] of 50 bleeding images with their corresponding ground truths are considered. The proposed scheme is implemented with m =

Table 11
Comparison of classification accuracy among different methods. LBP = local binary pattern.

Parameter	Uniform LBP [15]	Method in Ref. [24]	Method in Ref. [26]	Method in Ref. [28]	Proposed method without modeling	Proposed method
Sensitivity (%)	79.25	90.58	92.10	83.50	90.94	**97.55**
Specificity (%)	94.56	93.72	96.61	75.69	96.05	**96.59**
Accuracy (%)	91.50	92.58	95.85	77.15	95.54	**96.77**

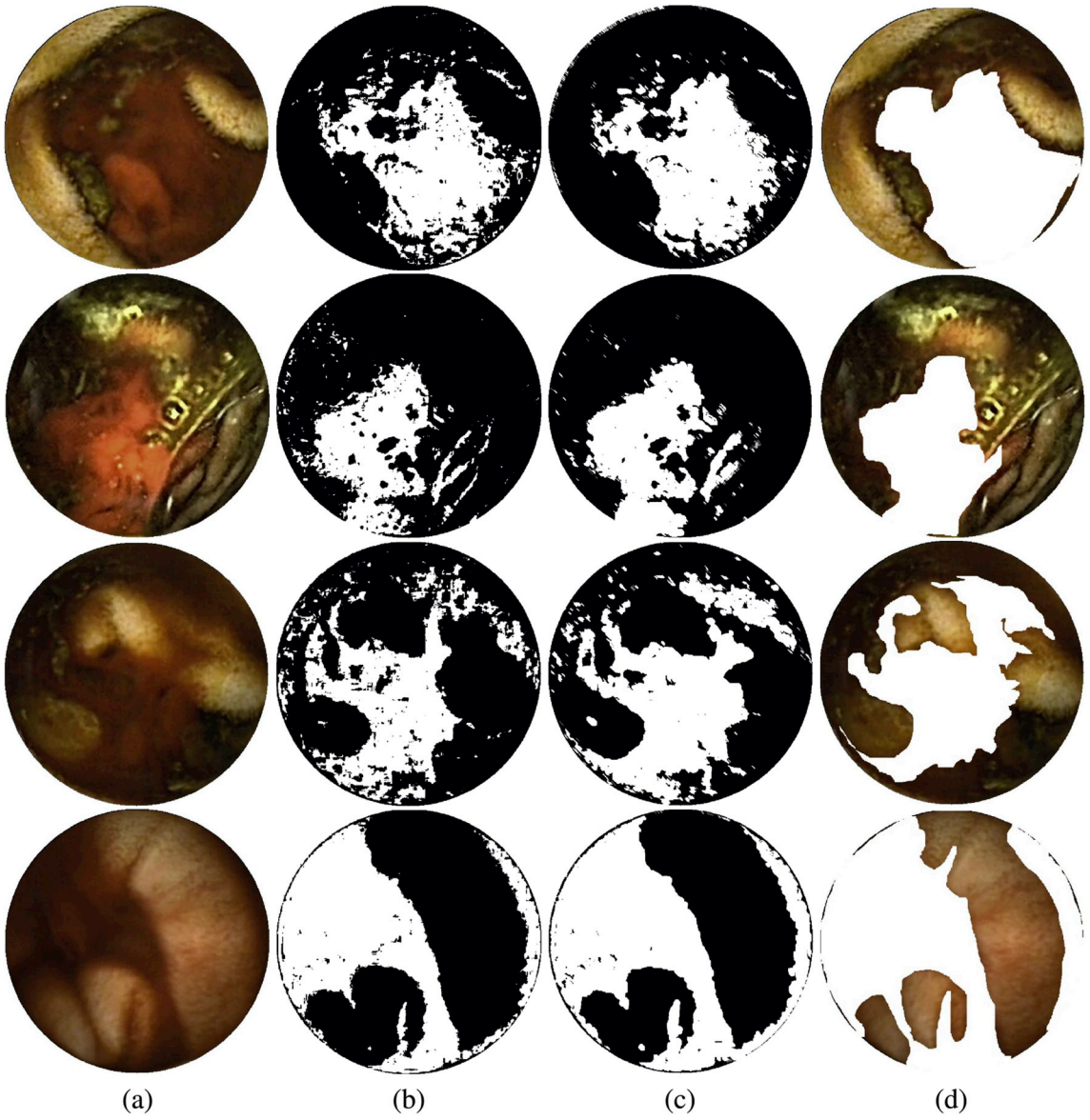

Fig. 11. Bleeding region detection. (a) Preprocessed bleeding image. (b) Extracted pixels of interest (POI). (c) Output bleeding region. (d) Ground truth image.

Table 12
Bleeding region detection performance using various values of p. FPR = false positive ratio; FNR = false negative ratio.

p	Precision	FPR	FNR
3	89.33%	5.15%	35.56%
5	88.81%	6.15%	31.10%
7	89.93%	6.84%	30.24%
9	**90.07%**	**6.83%**	**30.79%**
11	88.80%	08.07%	28.74%
13	89.02%	09.12%	28.35%

Table 13
Region detection performance using various K values. FPR = false positive ratio; FNR = false negative ratio.

K	Precision	FPR	FNR
2	**90.07%**	**6.83%**	**30.79%**
3	90.05%	6.31%	33.74%
4	89.98%	6.24%	33.97%
5	90.01%	6.03%	34.58%

Table 14
Comparison of different bleeding region detection methods. FPR = false positive ratio; FNR = false negative ratio.

Method	Precision	FPR	FNR
Method in Ref. [26]	85.03%	7.68%	38.13%
Method in Ref. [24]	88.38%	6.78%	33.13%
Proposed Method	**90.07%**	**6.83%**	**30.79%**

Table 15
Performance in continuous videos.

Clip No.	Sensitivity	Specificity	Accuracy
1	98.19%	97.45%	97.89%
2	85.32%	93.20%	87.95%
3	99.00%	–	99.00%
4	76.00%	82.67%	81.00%
5	75.00%	65.22%	66.00%

4.7, $n = 3.4$, and $p = 7$ using these 50 images, and the dice similarity coefficient (DSC) is found to be 0.87, whereas the DSC value of the methods proposed in Refs. [16,42] are 0.81 and 0.84, respectively. Therefore, the proposed scheme performs better than the two state-of-the-art methods.

3.6. Performance in continuous wireless capsule endoscopy (WCE) videos

In order to evaluate the performance of the proposed scheme, five sample continuous WCE video clips are reported. Here, the performance is measured in terms of sensitivity, specificity, and accuracy using a leave-one-out cross-validation scheme. Here, the POI are extracted using $m = 3.25$ and $n = 2.25$, and the Rayleigh PDF is used for modeling the POI statistics. The results are demonstrated in Table 15. For Clip number 3 specificity is undefined as it contains only bleeding images. The performance in continuous videos demonstrates how the proposed method performs when a single test video of a separate individual patient occurs. The result indicates the satisfactory performance of the proposed PDF fitting based feature extraction scheme in continuous WCE videos.

4. Conclusion

The main contribution of this paper lies in the fitting of a characteristic PDF suitable for modeling the extracted POI statistics. The nature of bleeding and non-bleeding images can be represented precisely with the help of the PDF fitting-based approach. The use of POI in calculating the PDF fitted parameters involves less computation, as well as ensuring more exact representations of bleeding. In particular, the Poisson, Rayleigh, and exponential PDF-fitted parameters of POI statistics are found to be very prominent for bleeding detection. It is experimentally found that the PDF fitting of POI statistics, instead of POI intensities, improves the classification performance to a good extent. Therefore, the PDF fitted parameters of POI statistics are used in the proposed feature vector. Performance of the proposed scheme in classifying bleeding and non-bleeding images are evaluated in terms of accuracy, specificity, and sensitivity, and it turns out that the proposed method outperforms the four other methods in terms of all performance indices. Then, bleeding regions are extracted using an unsupervised clustering based scheme which re-examines the probable bleeding candidates. This scheme increases the performance of the proposed bleeding zone localization as more probable bleeding pixels are incorporated in the bleeding region. Moreover, the scheme involves only a few computations, which is essential for real-time implementation. Morphological operations in zone localization help to make the bleeding region smooth. Finally, the performance in continuous videos ensures the goodness of the proposed PDF fitting based feature extraction scheme. Therefore, the proposed automatic bleeding image detection and bleeding region extraction scheme greatly can help physicians in diagnosing GI bleeding using WCE technology.

Acknowledgment

The authors would like to express their sincere gratitude to Dr. M. G. Kibria and Dr. S. N. F. Rumi of Dhaka Medical College and Hospital, for helping us in providing the ground truth of bleeding images and bleeding regions.

References

[1] D.G. Adler, C.J. Gostout, Wireless capsule endoscopy, Hosp. Physician 39 (5) (2003) 14–22.
[2] M. Coimbra, M. Mackiewicz, M. Fisher, C. Jamieson, J. Scares, J.S. Cunha, Computer vision tools for capsule endoscopy exam analysis, Eurasip Newsl. 18 (1) (2007) 1–19.
[3] R. Eliakim, Video capsule endoscopy of the small bowel, Curr. Opin. Gastroenterol. 24 (2) (2008) 159–163.
[4] G. Iddan, G. Meron, A. Glukhovsky, Wireless capsule endoscopy, Nature 405 (2000), 417–417.
[5] D.O. Faigel, D.R. Cave, Capsule Endoscopy, Saunders Elsevier, 2008, pp. 1–233.
[6] Y. Chen, J. Lee, A review of machine-vision-based analysis of wireless capsule endoscopy video, Diagn. Ther. Endosc. (2012) 1–9, 2012.
[7] J.M. Buscaglia, et al., Performance characteristics of the suspected blood indicator feature in capsule endoscopy according to indication for study, Clin. Gastroenterol. Hepatol. 6 (2008) 298–301.
[8] S.C. Park, et al., Sensitivity of the suspected blood indicator: an experimental study, World J. Gastroenterol. 18 (2012) 4169–4174.
[9] C. Signorelli, F. Villa, E. Rondonotti, C. Abbiati, G. Beccari, R. Franchis, Sensitivity and specificity of the suspected blood identification system in video capsule enteroscopy, Endoscopy 37 (2005) 1170–1173.
[10] S. Sainju, F.M. Bui, K. Wahid, Automatic bleeding detection in wireless capsule endoscopy videos using statistical features and region growing, J. Med. Syst. 38 (2014) 1–11.
[11] P. Guobing, Y. Guozheng, Q. Xiangling, C. Jiehao, Bleeding detection in wireless capsule endoscopy based on probabilistic neural network, J. Med. Syst. 35 (2011) 1477–1484.
[12] D.K. Iakovidis, A. Koulaouzidis, Automatic lesion detection in capsule endoscopy based on color saliency: closer to an essential adjunct for reviewing software, Gastrointest. Endosc. 80 (5) (2014) 877–883.
[13] P. Sivakumar, B.M. Kumar, A Novel Method to Detect Bleeding Frame and Region in Wireless Capsule Endoscopy Video, Cluster Computing, 2018, pp. 1–7.
[14] Y. Fu, W. Zhang, M. Mandal, M.Q.H. Meng, Computer-aided bleeding detection in WCE video, IEEE J. Biomed. Health Inf. 18 (2014) 636–642.
[15] B. Li, M.Q.H. Meng, Computer-aided detection of bleeding regions for capsule endoscopy images, IEEE Trans. Biomed. Eng. 56 (2009) 1032–1039.
[16] E. Tuba, M. Tuba, R. Jovanovic, An algorithm for automated segmentation for bleeding detection in endoscopic images, in: Proc. International Joint Conference on Neural Networks, IJCNN), 2017, pp. 4579–4586.
[17] X. Jia, M.Q.-H. Meng, A deep convolutional neural network for bleeding detection in wireless capsule endoscopy images, in: Proc. 2016 38th Annual International Conference of the IEEE Engineering in Medicine and Biology Society (EMBC), IEEE, 2016, pp. 639–642.
[18] P. Coelho, A. Pereira, M. Salgado, A. Cunha, A deep learning approach for red lesions detection in video capsule endoscopies, in: Proc. International Conference Image Analysis and Recognition, Springer, 2018, pp. 553–561.
[19] X. Jia, M.Q.-H. Meng, A study on automated segmentation of blood regions in wireless capsule endoscopy images using fully convolutional networks, in: Proc. 2017 IEEE 14th International Symposium on Biomedical Imaging (ISBI 2017), IEEE, 2017, pp. 179–182.
[20] X. Hu, Y. Yuan, Deep-learning-based classification for DTM extraction from ALS point cloud, Remote Sens. 8 (9) (2016) 730.
[21] D. Ravì, C. Wong, F. Deligianni, M. Berthelot, J. Andreu-Perez, B. Lo, G.-Z. Yang, Deep learning for health informatics, IEEE J. Biomed. Health Inf. 21 (1) (2016) 4–21.
[22] T. Ghosh, S.A. Fattah, K.A. Wahid, W.-P. Zhu, M.O. Ahmad, Cluster based statistical feature extraction method for automatic bleeding detection in wireless capsule endoscopy video, Comput. Biol. Med. 94 (2018) 41–54.
[23] Y. Yuan, B. Li, M.Q.-H. Meng, WCE abnormality detection based on saliency and adaptive locality-constrained linear coding, IEEE Trans. Autom. Sci. Eng. 14 (1) (2016) 149–159.
[24] A.K. Kundu, S.A. Fattah, M.N. Rizve, An automatic bleeding frame and region detection scheme for wireless capsule endoscopy videos based on inter-plane intensity variation profile in normalized RGB color space, J. Healthc. Eng. (2018) 1–12, 2018.
[25] A.K. Kundu, M.N. Rizve, T. Ghosh, S.A. Fattah, A segmented color plane histogram based feature extraction scheme for automatic bleeding detection in wireless capsule endoscopy, in: Proc. 2016, IEEE Students' Technology Symposium, 2016, pp. 245–249.
[26] Y. Yuan, B. Li, M.Q.-H. Meng, Bleeding frame and region detection in the wireless capsule endoscopy video, IEEE J. Biomed. Health Inf. 20 (2) (2016) 624–630.
[27] M. Ramaraj, S. Raghavan, V. Raghunath, A.K. Wahid, Histogram variance controlled bleeding detectors for wireless capsule endoscopic images, J. Med. Imag. Health Info. 4 (2014) 500–510.
[28] S. Sainju, F.M. Bui, K. Wahid, Bleeding detection in wireless capsule endoscopy based on color features from histogram probability, in: Proc. IEEE Canadian Conf. On Electrical and Computer Engineering, 2013, pp. 1–4.
[29] A. Liaqat, M.A. Khan, J.H. Shah, M. Sharif, M. Yasmin, S.L. Fernandes, Automated ulcer and bleeding classification from wce images using multiple features fusion and selection, J. Mech. Med. Biol. 18 (04) (2018) 1850038.
[30] T. Ghosh, S.A. Fattah, K.A. Wahid, CHOBS: color histogram of block statistics for automatic bleeding detection in wireless capsule endoscopy video, IEEE J. Transl. Health Med. 6 (2018) 1–12.
[31] The capsule endoscopy website. https://www.medtronic.com/covidien/en-us/products/capsule-endoscopy.html, 2014.
[32] A. Papoulis, S.U. Pillai, Probability, Random Variables, and Stochastic Processes, fourth ed., Tata McGraw-Hill Education, 2002.
[33] D. Freedman, P. Diaconis, On the histogram as a density estimator: L 2 theory, Probab. Theory Relat. Fields 57 (4) (1981) 453–476.
[34] V.N. Vapnik, Statistical Learning Theory, Wiley, 1998.
[35] T. Kanungo, D.M. Mount, N.S. Netanyahu, C.D. Piatko, R. Silverman, A.Y. Wu, An efficient k-means clustering algorithm: analysis and implementation, IEEE Trans. Pattern Anal. Mach. Intell. 24 (7) (2002) 881–892.
[36] R. Gonzalez, R. Woods, Digital Image Processing, Prentice Hall, NJ, USA, 2008.
[37] H. S. Bhat, N. Kumar, On the Derivation of the Bayesian Information Criterion, School of Natural Sciences, University of California.

[38] C. Thornton, Separability is a learner's best friend, in: 4th Neural Computation and Psychology Workshop, Springer, 1998, pp. 40–46.
[39] J. Greene, Feature subset selection using thornton's separability index and its applicability to a number of sparse proximity-based classifiers, in: Proc. Annual Symposium of the Pattern Recognition Association of South Africa, 2001.
[40] D.G. Altman, J.M. Bland, Diagnostic tests 1: sensitivity and specificity, Biomed. J. 308 (1994) 1552.
[41] F. Conversano, R. Franchini, C. Demitri, L. Massoptier, M. A, et al., Hepatic vessel segmentation for 3D planning of liver surgery: experimental evaluation of a new fully automatic algorithm, Acad. Radiol. 18 (2011) 461–470.
[42] F. Deeba, F.M. Bui, K.A. Wahid, Automated growcut for segmentation of endoscopic images, in: Proc. 2016 International Joint Conference on Neural Networks (IJCNN), IEEE, 2016, pp. 4650–4657.
[43] F. Deeba, Bleeding images and corresponding ground truth of CE images. https://sites.google.com/site/farahdeeba073/Research/resources, 2016.